Circulation and melting beneath George VI Ice Shelf, Antarctica

Adrian Jenkins[1] and Stan Jacobs[2]

[1] Oceanographic data are presented from the eastern Bellingshausen Sea, representing the first near-contemporaneous sampling of conditions near both the northern and southern ice fronts of George VI Ice Shelf. Circumpolar Deep Water (CDW) with a temperature in excess of 1°C floods the entire continental shelf and forms the main inflow to the cavity beneath the ice shelf. We use measurements of salinity, potential temperature, stable isotope ratios and dissolved oxygen, helium, and neon to show that the outflows contain meltwater in concentrations that rise to a maximum of around 3%. Assuming that the currents are in geostrophic balance, we calculate relative velocities along the ice front sections, then estimate the absolute velocity by inversion of the tracer conservation equations. We obtain an overall mean melt rate of $3-5$ m a^{-1} and a net south-to-north throughflow beneath the ice shelf of $0.17-0.27$ Sv. The mean melt rate exceeds that required for equilibrium, consistent with recent observations of ice shelf thinning and retreat. Melting beneath the ice shelf drives upwelling of about 0.1 Sv in total of CDW into the surface mixed layer at the two ice fronts. The effective vertical heat flux per unit area of ice shelf cover is 8 W m^{-2}, more than 4 times that estimated for vertical diffusion through the main pycnocline of the neighboring open water region. The south-to-north throughflow carries a particularly strong signature of upwelled CDW, including low dissolved oxygen and high nutrient concentrations, north into Marguerite Bay.

1. Introduction

[2] George VI Ice Shelf is the largest and most studied of the west Antarctic Peninsula ice shelves. It occupies a large part of George VI Sound, a Cenozoic rift separating the western coast of Palmer Land from the eastern coast of Alexander Island (Figure 1). The northern part of the sound was first charted during the British Graham Land Expedition of 1934–1937, while its southern extent was revealed during the United States Antarctic Service Expedition of 1939–1941. Through the latter half of the 20th century a series of research stations were established around the northern coast of Marguerite Bay, allowing near-continuous occupation of the region. George VI Sound and Ice Shelf became convenient targets for summer field expeditions, with research focused on the geological origin of the sound and the processes controlling the mass budget of the ice shelf. Although the presence of an ice shelf within a narrow channel, open at both ends, is often regarded as being unusual, the configuration is topologically similar to other ice shelves. Filchner-Ronne Ice Shelf, for example, also occupies a deep, albeit much broader channel around the southern part of Berkner Island, and many, if not most, other ice fronts are split by one or more islands.

[3] Within George VI Sound the ice shelf covers an area of approximately 25,000 km^2 [*Potter and Paren*, 1985]. It reaches a maximum thickness of around 500 m about 70 km from the southern ice front, where a ridge of thick ice extends across the sound (near 70°W). The vast majority (96–97%) of the flow into the ice shelf comes from Palmer Land while surface accumulation also makes a significant contribution (~20%) to its mass budget [*Potter et al.*, 1984]. The northern ice front, which faces Marguerite Bay, appears to be near the geographical limit of ice shelf viability and has undergone a gradual retreat in recent decades [*Lucchitta and Rosanova*, 1998], a timeframe over which much of the nearby Wordie Ice Shelf disintegrated [*Doake and Vaughan*, 1991]. There is extensive surface melting over the northern parts of the ice shelf and much of the ice column near the northern ice front appears to be temperate [*Paren and Cooper*, 1986]. Ponding of meltwater occurs at the surface in summer, but only a small quantity (0.4 ± 0.2 km^3) appears to drain each year via moulins and tide cracks to the underlying ocean [*Reynolds*, 1981]. This is less than 1% of the annual mass input to the ice shelf [*Potter et al.*, 1984]. Although summer melting has almost certainly increased since these estimates were made, drainage of meltwater probably remains an insignificant part of the overall mass budget. Conditions in the south, where the ice front faces into Ronne Entrance, are colder and the ice front position appears to be relatively steady at present. There is some

[1]British Antarctic Survey, Natural Environment Research Council, Cambridge, UK.
[2]Lamont-Doherty Earth Observatory of Columbia University, Palisades, New York, USA.
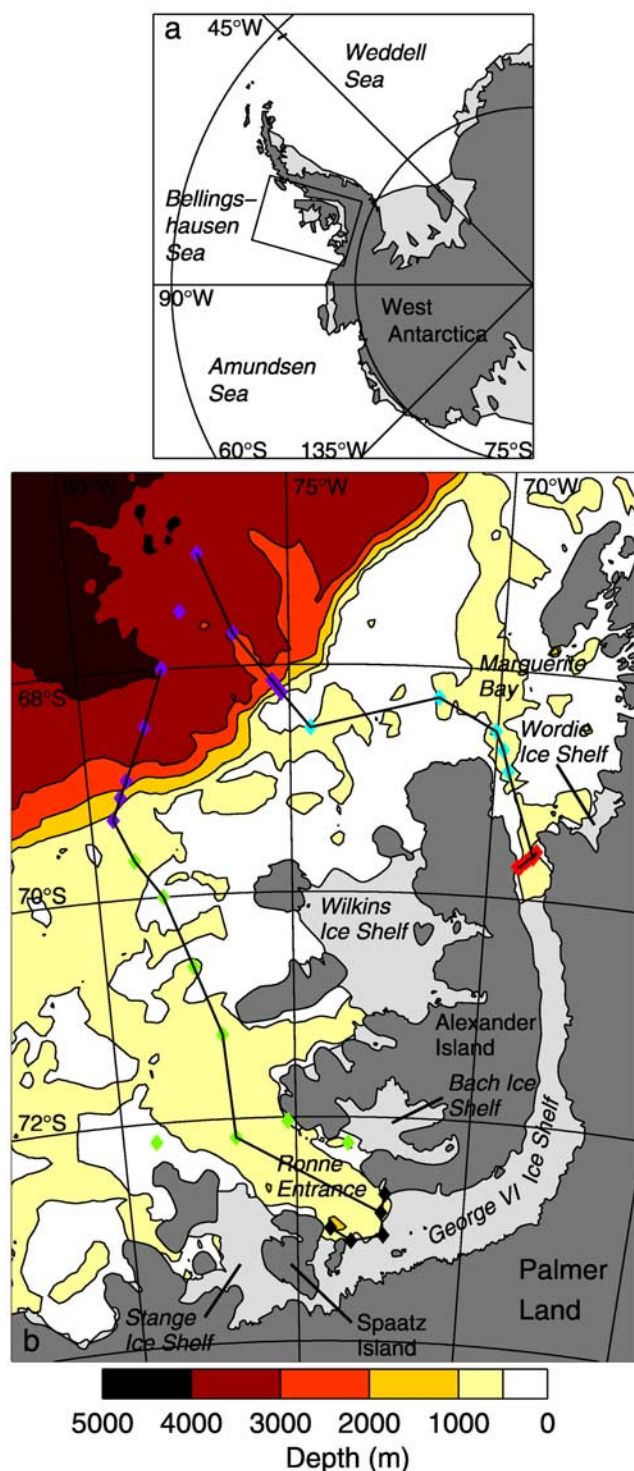
Figure 1. (a) Map of the Amundsen/Bellingshausen sector of Antarctica showing the area enlarged in Figure 1b. (b) Map of George VI Ice Shelf and adjacent continental shelf showing the location of CTD stations discussed in the paper. The colors associated with each station marker are used in subsequent diagrams to indicate groupings of deep ocean (magenta), continental shelf (north, cyan; south, green) and ice front (north, red; south, black) stations. Solid lines connecting station markers indicate the sections plotted in Figures 2 and 4. At the time of the study fast ice occupied the area between the northern ice front section and the ice shelf.

evidence at the margins of the ice shelf to suggest that it may have disappeared completely during the early to mid-Holocene before reforming [*Sugden and Clapperton*, 1981; *Hjort et al.*, 2001; *Bentley et al.*, 2005].

[4] Both northern and southern ice fronts abut embayments of the Bellingshausen Sea, where almost unmodified Circumpolar Deep Water (CDW) floods the continental shelf [*Talbot*, 1988]. As a result, water temperatures close to George VI Ice Shelf exceed 1°C, giving rise to rapid basal melting [*Bishop and Walton*, 1981; *Lennon et al.*, 1982]. *Potter et al.* [1984] estimated an equilibrium basal melt rate of 2.1 m a^{-1}, averaged over the entire ice shelf. At this rate basal melting removes all but 8% of the mass input to the ice shelf from glacier discharge and surface accumulation. The ice is therefore derived almost exclusively from local accumulation by the time it reaches the ice fronts. Although the ridge of thickest ice near 70°W effectively divides the upper water column into northern and southern regions, *Potter et al.* [1984] found no significant difference between the equilibrium melt rates in these two regions. Similar oceanographic conditions have apparently persisted on the Bellingshausen Sea continental shelf throughout the observational era, begun during the Belgian Antarctic Expedition of 1897–99 [*Arctowski and Mill*, 1908], although the record is temporally and spatially sparse. Observations of current ice shelf thinning (A. Shepherd, personal communication, 2007) and retreat of the northern ice front imply that the present ice shelf is not in equilibrium with today's oceanographic regime. Further west on the Amundsen Sea continental shelf, ice shelf thinning [*Shepherd et al.*, 2004] has been linked with the presence of CDW on-shelf [*Jacobs et al.*, 1996].

[5] During the 1980s a program of research was conducted into the interactions between the ice shelf and the underlying CDW in George VI Sound. The main findings were summarized by *Potter and Paren* [1985]. The work was focused predominantly near the northern ice front, where rifts in the ice shelf allowed easy access for oceanographic instruments lowered into the water column. The circulation proposed was one in which CDW was drawn beneath the ice shelf, where melting drove upwelling and an outflow that was concentrated in the west. *Potter et al.* [1988] added some more detail to this picture, deriving geostrophic velocities from a temperature and salinity section measured along the northern ice front. They found weak flow (<2 cm s^{-1}) over much of the section with a number of inflows, near the eastern margin and the seabed, balancing an intense surface outflow in the west. *Potter et al.* [1988] also discussed measurements made at the southern ice front, but these were more scattered and the single continuous section included only temperature data.

[6] In March 1994 we obtained oceanographic measurements, including continuous profiles of temperature, salinity and dissolved oxygen as well as discrete point observations of the oxygen isotope ratio and dissolved helium and neon concentrations, at both the northern and southern ice fronts of George VI Ice Shelf (Figure 1) from the research icebreaker *Nathaniel B Palmer* [*Giulivi and Jacobs*, 1997; *Hohmann et al.*, 2002]. These data represent the most complete, near-contemporaneous sampling of conditions at both ice fronts that has been made to date. Here we discuss the data and show how they can be used to estimate the

concentration of meltwater derived from the ice shelf that is present in the water column. We then derive relative geostrophic velocities across each section from the density data and use the inverse method described by *Wunsch* [1978] to constrain our estimated absolute velocities such that overall transports into and out of the sub-ice-shelf cavity are balanced. We investigate how well this technique enables us to evaluate the ocean circulation and net meltwater production rate within the cavity. Our aims are to quantify the transport of CDW toward and meltwater away from the ice shelf and to compare the net melt rate with that required for equilibrium.

2. Continuous Profile Data

[7] The oceanographic sections discussed in this paper were occupied during cruise NBP9402 to the Amundsen and Bellingshausen seas. Acquisition and processing of these data are described by *Giulivi and Jacobs* [1997]. We converted the dissolved oxygen data to mL kg^{-1}, and calculated and removed a pressure-weighted mean residual between bottle and downcast profile data for each station individually. This minimizes the effect of larger near-surface offsets that may result from upcast sampling, and affords more weight to titration consistency than to sensor stability. The remaining root mean square residual below 150 m depth is 0.05 mL kg^{-1}. Although we focus our attention primarily on the sections obtained near George VI ice fronts, we set those data in their wider context by reference to other oceanographic stations occupied during the same cruise in the eastern Bellingshausen Sea (Figure 1). The stations comprising the southern ice front section were located a few hundred meters seaward of the ice front and were occupied over a 14 h period on 24 March, while those that form the northern ice front section were occupied over a 13 h period on 30/31 March while the ship was up against a fast ice edge, about 40 km north of the actual ice front.

[8] The main feature of the water column in this region is the ubiquitous presence of CDW, characterized by relatively high temperature and salinity and low dissolved oxygen concentration, which appears to access all the deeper regions of the continental shelf (Figure 2). Although the plotted sections may not follow the access routes, they suggest that CDW flows onto the shelf both in the north (Marguerite Bay) and in the south (Ronne Entrance). Not clear from the contouring is the fact that the highest temperatures recorded in Marguerite Bay are ∼0.1°C higher than those found in Ronne Entrance. However, the warmest, most saline waters do not appear to reach the northern ice front. The main bathymetric trough in Marguerite Bay originates from George VI Sound, but near 69°S it is at least partially blocked by a ridge of higher ground extending northeast from the coast of Alexander Island [*O'Cofaigh et al.*, 2005]. Station 157 (Figure 2) was located on part of this ridge. There appears to be only one narrow gap in the ridge where the seabed dips to around 1000 m for a few kilometers, and this may be insufficient to allow a significant southward flow of the deepest CDW from the north. The station immediately south of the ridge (number 156) has a mid-depth intrusion of northern CDW, shown clearly in the temperature profiles of Figure 3. These are strongly suggestive of northern CDW spilling over and around seabed topography in small enough quantities that the whole of George VI Sound may dominated by CDW flowing in from the south.

[9] Although the deep water column at both ice fronts has similar characteristics, waters found immediately below the near freezing surface layer at the northern ice front are saltier, warmer and lower in dissolved oxygen than those at the southern ice front (Figure 4). The dissolved oxygen signature is the most marked and is a clear indicator that the reason for these upper water column differences is the upwelling of CDW at the northern ice front. The impact of the upwelling can be traced well beyond the ice front, out into Marguerite Bay (Figure 2). Although less pronounced, there is a similar signature of upwelling seaward of the southern ice front, and at both ice fronts it is strongest in the west. We would anticipate seeing concentrated outflows from beneath the ice shelves on the western side of the cavity openings and will argue that the presence of CDW-like characteristics in the upper water column is a result of upwelling driven by melting at the base of the ice shelf.

[10] In potential temperature/salinity space (Figure 5a) the far-field stations on the outer continental shelf and beyond the shelf break show the usual trends from CDW core characteristics ($\theta > 1$°C, S ≈ 34.7) to remnant Winter Water (WW, $\theta \approx -1.7$°C, S ≈ 34), and from WW to more variable, warmer and fresher, surface waters. There is a pronounced cooling of the CDW as it crosses the shelf break (Figure 2), brought about by the erosion of the temperature maximum layer, but other than that the water column changes little until it feels the influence of the ice shelves. At the southern ice front the impact of meltwater is manifested counter-intuitively in the warm, salty intrusions that interrupt the θ/S trend in the main CDW/WW thermocline (Figure 5a). The warm/salty extremes of these intrusions have the characteristics of glacier ice melting into the CDW found at the southern ice front, suggesting that they were formed by melt-driven upwelling of CDW beneath the ice shelf. *Potter et al.* [1988] found similar melt-driven intrusions at the southern ice front, while the origins of analogous features in the Amundsen Sea were discussed in more detail by *Hellmer et al.* [1998] and *Jenkins* [1999]. At the northern ice front the CDW/WW thermocline is absent and the whole water column below the shallow surface layer has the characteristics of ice melting into CDW, as noted before by *Potter and Paren* [1985] and *Potter et al.* [1988]. The same trend in properties dominates the mid-water column of several of the far-field stations in Marguerite Bay, suggesting a key role for outflows from beneath the ice shelf in setting the properties of waters in the bay. All the on-shelf data, with the exception of the low-salinity surface layer, have θ/S values intermediate between the CDW/WW and the CDW/meltwater trends. Properties of the CDW endpoint at the northern ice front (Figure 5b) show that it can be related to waters found at the southern ice front. The warmer CDW from Marguerite Bay is absent at the northern ice front, both in its pure form and as a contributor to CDW/meltwater mixtures.

[11] In dissolved oxygen/salinity space (Figure 5c) we can identify similar characteristics, although in this case the difference between the ambient CDW/WW water column and the CDW/meltwater mixtures generated beneath the ice shelf is even more marked. The inflowing CDW on the
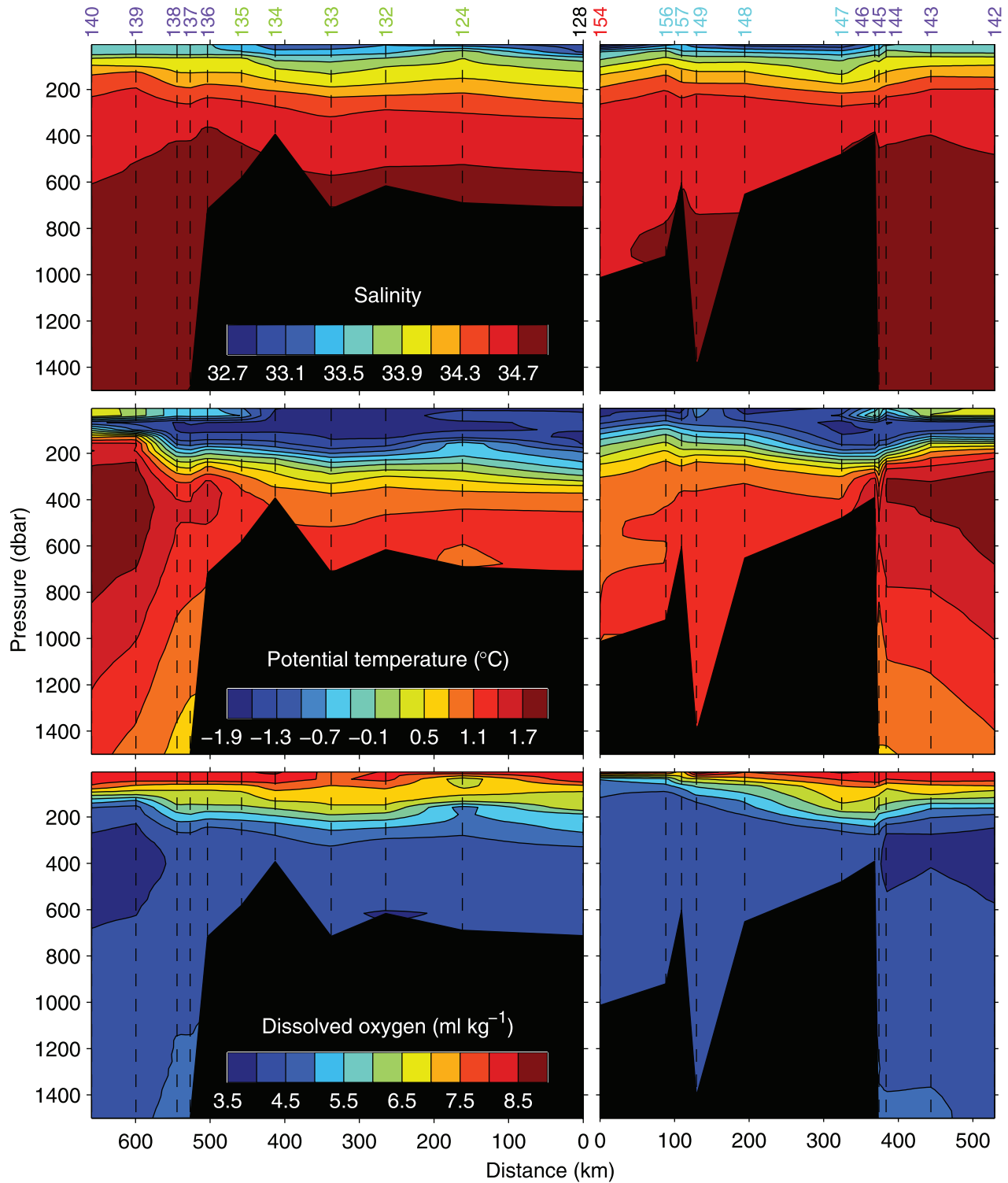
Figure 2. (top) Salinity, (middle) potential temperature, and (bottom) dissolved oxygen recorded in March 1994 along sections running from the (left) southern and (right) northern ice fronts across the continental shelf and into the deep ocean (see Figure 1 for station locations). The sections start and end at a CTD station and intermediate stations are indicated by the vertical dashed lines (numbered along the top of the plot with the same color coding as used in Figure 1).

outer continental shelf and beyond is associated with a dissolved oxygen minimum ($O_2 \approx 4$ mL kg^{-1}, S $\approx$ 34.7) that is eroded as the water flows onto the shelf. Above this there is an approximate linear trend toward WW values

($O_2 \approx 6.5$ mL kg^{-1}, S $\approx$ 34), which persists, albeit with more scatter into the surface waters where the dissolved oxygen concentration is close to saturation. When ice melts from the base of the ice shelf, the oxygen contained within
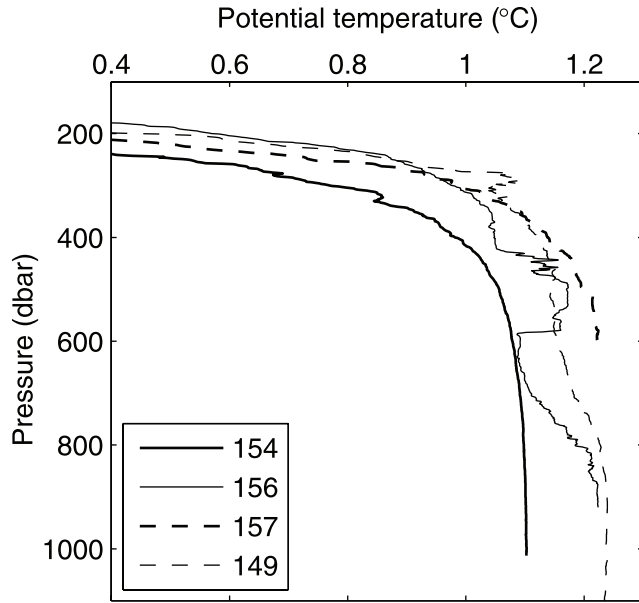
Figure 3. Potential temperature measured between 200 and 1000 dbar at the northern ice front (station 154) and three far-field stations in the north (see Figures 1 and 2 for locations). Stations 156 and 149 lie to the south and north, respectively, of a shallower bank, over which station 157 is positioned.

the air bubbles trapped in the ice goes into solution. However, the dissolved oxygen levels that result from this process are significantly lower than those obtained by equilibration with the atmosphere. Thus the northern ice front stations are immediately obvious in Figure 5c, the linear trend being characteristic of CDW mixing with glacier meltwater. At any particular salinity such mixtures have much lower dissolved oxygen concentrations than the ambient water column. Although the northern ice front data are suggestive of two distinct trends, generated by mixing with meltwater having slightly differing properties, this is an artifact of the continuous profile data caused by a nonuniform response of the dissolved oxygen sensor to changes in pressure. Oxygen concentrations measured by Winkler titrations performed on bottle samples all plot on the upper trend line. As in Figure 5a the southern ice front profiles and several from further afield show the ambient O_2/S trend, interrupted by oxygen poor intrusions that are mixtures of CDW and meltwater, analogous to features reported by *Jenkins* [1999] in the Amundsen Sea, while several of the northern far-field stations follow the simple CDW/meltwater mixing line over much of the water column. Processes other than mixing, equilibration with the atmosphere and addition of meltwater can also influence concentrations of dissolved oxygen, and biological activity could be responsible for some of the scatter seen in the properties of the upper water column. However, the meltwater signature is sufficiently clear, particularly below the surface layers, that we can treat dissolved oxygen as a conservative tracer when it comes to quantifying the concentrations of meltwater in the water column.

[12] In Figure 5d we plot the data in dissolved oxygen/potential temperature space. Again we can distinguish

ambient (CDW/WW) and melt-induced (CDW/meltwater) trends that envelop virtually all the on-shelf values. Only in the near surface layers, where equilibration with the atmosphere takes the dissolved oxygen values toward saturation do the data lie outside this envelope. The mixing line gradients in Figure 5d are simply the gradient ratios of the analogous lines plotted in O_2/S and θ/S space (Figures 5a and 5c). Obtaining consistent fits with the data in all three cases was the guiding principle behind our heuristic choice of characteristic linear trends.

3. Meltwater Concentrations

[13] The next step in our analysis of the data is to quantify the concentration of meltwater in the water column. At the northern ice front this is a comparatively straightforward task, since the water column is for the most part a simple two-component mixture of CDW and meltwater. We could therefore write a simple conservation equation for any tracer, χ, which could be any of the continuously or discretely sampled properties

$$\chi_{mix} = (1 - \varphi)\chi_{CDW} + \varphi\chi_{melt}, \qquad (1)$$

from which the meltwater fraction, φ, could be calculated:

$$\varphi = \frac{\chi_{mix} - \chi_{CDW}}{\chi_{melt} - \chi_{CDW}}. \qquad (2)$$

However, at the southern ice front the situation is more complex in that WW, with varying properties, is present in significant quantities, and mixes with CDW to form the waters of the main pycnocline. Hence we cannot treat the entire water column as if it were a simple two-component mixture of CDW and meltwater. Since we have measurements of more than one tracer we could write a set of two equations, analogous to equation (1), for the unknown fractions of meltwater and WW in the three-component mix. An alternative, but equivalent, approach is that adopted by *Jenkins* [1999]. We define a composite of two tracers:

$$\psi^{2,1} = \left(\chi^2 - \chi^2_{CDW}\right) - \left(\chi^1 - \chi^1_{CDW}\right)\left(\frac{\chi^2_{WW} - \chi^2_{CDW}}{\chi^1_{WW} - \chi^1_{CDW}}\right), \qquad (3)$$

this being the difference between the actual value of tracer 2 and the value that would be measured in a simple two-component mixture of CDW and WW that had the same concentration of tracer 1. The great value of the composite tracer is that its concentration is by definition zero for any two-component mixture of CDW and WW. We can then calculate the meltwater fraction directly using the composite tracer in equation (2), which now takes the form:

$$\varphi = \frac{\psi^{2,1}_{mix}}{\psi^{2,1}_{melt}}. \qquad (4)$$

This approach makes it explicit how our choice of a single value for the concentrations of each of the two tracers in the WW influences our derived meltwater fractions. In fact the concentrations themselves are unimportant, provided the gradient of the line connecting
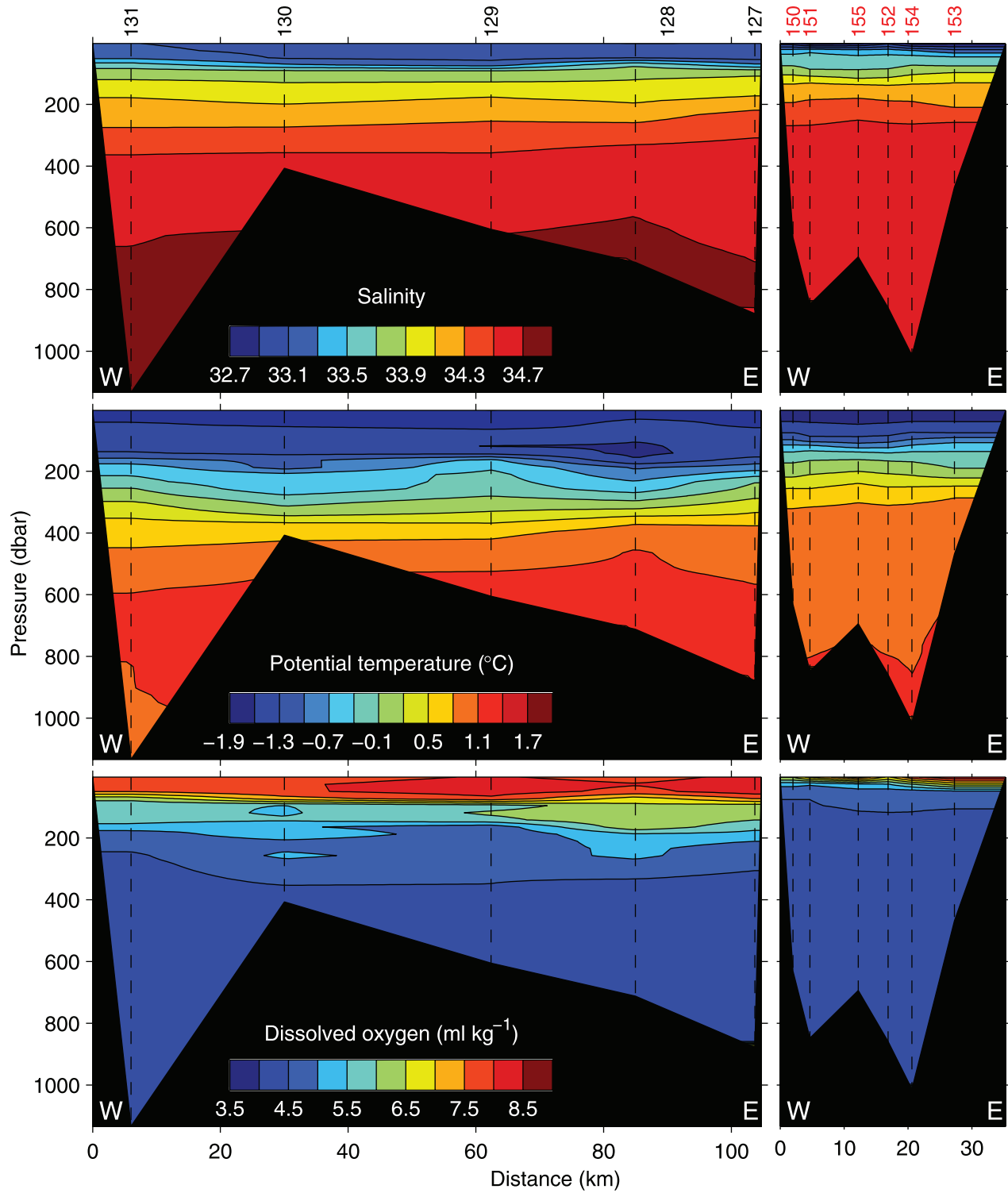
Figure 4. (top) Salinity, (middle) potential temperature, and (bottom) dissolved oxygen recorded in March 1994 at the (left) southern and (right) northern ice fronts. Both sections are drawn looking out from beneath the ice shelf. CTD stations are indicated by the vertical dashed lines (numbered along the top of the plot with the same color coding as used in Figure 1).

the WW properties to the less variable CDW properties on a plot of tracer 1 versus tracer 2 (last term in parentheses in equation (3)) is unchanged. This line defines a contour of zero meltwater fraction and all other contours of equal meltwater fraction lie parallel to it (Figure 5). Note that there

are two cases in which equation (4) reduces to equation (2). The first is the more obvious, when the WW/CDW trend has zero slope, i.e., when:
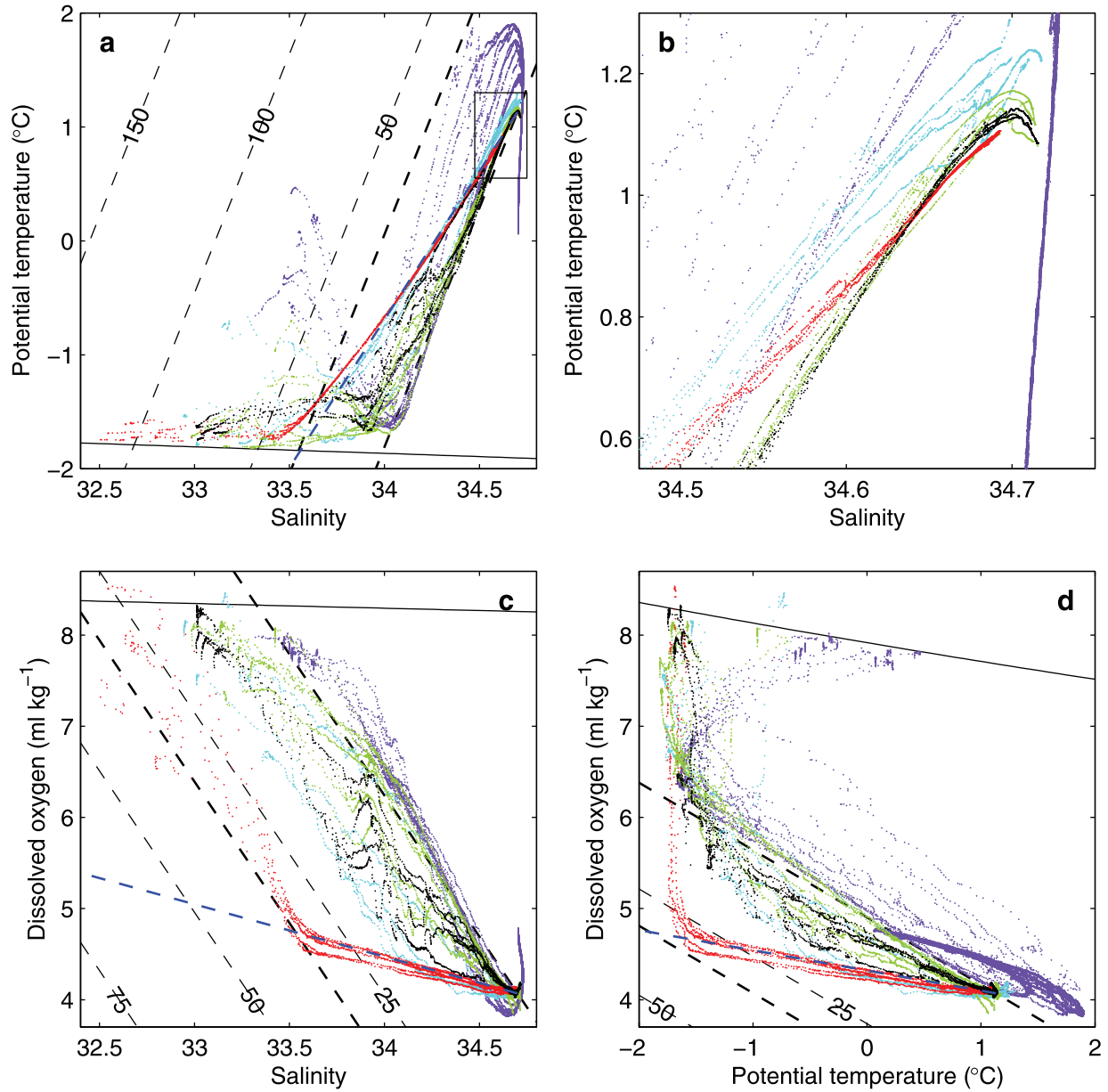
$$\chi^2_{WW} = \chi^2_{CDW}, \tag{5}$$

Figure 5. (a, b) The θ/S, (c) O_2/S, and (d) O_2/θ data obtained at the stations marked in Figure 1. Color coding of the individual stations corresponds to that indicated in Figure 1. The small box around (34.6, 1°C) in Figure 5a is shown enlarged in Figure 5b. In all cases the numbered, light dashed lines are contours of meltwater fraction (per mille), while the bold dashed lines indicate the theoretical upper bound on the melt fraction and the CDW/WW trend used to define the zero melt fraction contour. The blue dashed lines indicate the CDW/meltwater mixing trends. The near-horizontal solid lines indicate the surface freezing point (Figure 5a) and saturation concentrations for water at the surface freezing point (Figure 5c) and at a salinity of 33.5 (Figure 5d).

or in other words tracer 2 has a constant value in the ambient water column. The second is when the data lie on the CDW/meltwater mixing line, in which case the properties are related as follows:

$$\left(\chi^1 - \chi^1_{CDW}\right) = \left(\chi^2 - \chi^2_{CDW}\right)\left(\frac{\chi^1_{melt} - \chi^1_{CDW}}{\chi^2_{melt} - \chi^2_{CDW}}\right) \quad (6)$$

and substitution of equation (6) into equations (3) and (4) yields equation (2). Thus for simple two-component

mixtures of meltwater and CDW equations (2) and (4) are algebraically identical.

[14] In order to put a numerical value on the contours of meltwater fraction in Figure 5 we need to evaluate the denominator in equation (4), and for this we need to know the values of the individual tracers in the meltwater. The northern ice front profiles are dominated by simple two-component mixtures of CDW and melt, which lie along an approximately straight mixing line. Since the meltwater is fresh, we can find the other tracer values simply by

extrapolation of the mixing (blue dashed) lines shown in Figure 5 to zero salinity. We obtain a temperature of $-89°C$ and a dissolved oxygen concentration of 24 mL kg^{-1}. These numbers may at first look surprising, but they have a physical explanation [see also *Hellmer et al.*, 1998; *Jenkins*, 1999].

[15] On polar ice sheets, snow that falls on the surface is transformed into firn then ice by a process of compaction. The voids within the firn are air-filled, and the interconnectivity of these air pockets is reduced as the firn is compressed. The permeability falls to zero when the pore volume is around 130 mL kg^{-1} [*Martinerie et al.*, 1992]. The actual volume of air contained within the voids, measured at standard temperature and pressure (STP), will depend on the temperature and atmospheric pressure at the site of formation of the ice. Within the catchment basin of George VI Ice Shelf the ice sheet elevation is relatively low and the air temperature is relatively high. The net effect might be to reduce the volume of air at STP by about 10% [*Martinerie et al.*, 1992]. Since the air is 21% oxygen, we should expect to see a dissolved oxygen concentration of around 24 to 25 mL kg^{-1} in the meltwater. This is about three times the saturation level in seawater at low temperature and atmospheric pressure, but at the elevated pressures found beneath the ice shelf all the gas goes into solution. Our inferred meltwater concentration therefore seems reasonable and provides support for our slightly uncertain extrapolation of the O$_2$/S mixing line.

[16] Salt and dissolved oxygen are conserved during the melting process such that the mass of each in the melt is identical to that in the solid ice. However, when dealing with potential temperature it is the conservation of energy that we must consider, and in particular we must take into account the energy given up by the ocean to effect the phase change. For ice melting into CDW we can write the energy balance per unit mass as:

$$(1-\varphi)c_w(\theta_{CDW}-\theta_{mix}) = \varphi c_w(\theta_{mix}-\theta_f) + \varphi L + \varphi c_i(\theta_f-\theta_i), \quad (7)$$

where c_w and c_i are the specific heat capacities of seawater and ice respectively, L is the latent heat of fusion of ice, and θ_i and θ_f are the temperatures of the ice shelf and freezing point respectively. The term on the left hand side is the total energy lost by the CDW, while the terms on the right hand side represent the portion of that energy loss that is used respectively for warming the meltwater from the freezing point, melting the ice and warming the ice to the freezing point. Rearranging equation (7) we can write an expression analogous to equation (1):

$$\theta_{mix} = (1-\varphi)\theta_{CDW} + \varphi\theta_{melt}, \quad (8)$$

where:

$$\theta_{melt} = \theta_f - \frac{L}{c_w} - \frac{c_i}{c_w}(\theta_f-\theta_i). \quad (9)$$

Using equation (9) we can understand our effective meltwater temperature of $-89°C$ as the overall result of melting an ice shelf with a mean ice temperature, θ_i, of $-7.6°C$ and mixing the resulting meltwater into the ocean. This relatively high ice temperature reflects the low

elevation, warm catchment basin mentioned above and the fact that the far northern part of the ice shelf is temperate (i.e., at the pressure freezing point throughout) [*Paren and Cooper*, 1986].

[17] We are now in a position to calculate the meltwater concentration associated with each observation of salinity, potential temperature and dissolved oxygen, from the position of the data point in θ/S, O$_2$/S and O$_2$/θ space (Figure 5). We must attach caveats to these calculations. There is some uncertainty in defining linear trends associated with mixing in the main pycnocline and between CDW and a meltwater source that is assumed to be uniform. Any deviations from linearity introduce noise to the calculations. The assumption of approximate linearity breaks down completely in the surface mixed layer and the calculations are invalid there. Equilibration with the atmosphere raises the dissolved oxygen concentration toward saturation, while other sources of freshwater reduce the salinity, without significantly altering the temperature. In O$_2$/S space the processes of freshening and equilibration tend fortuitously to compensate each other, so that the apparent meltwater fraction stays roughly constant through the surface layers, while calculations based on θ/S data are biased high in the surface layers and those based on O$_2$/θ data are biased low. We therefore regard the O$_2$/S data as providing our most reliable estimates of meltwater fraction and use the scatter of the other two calculations (i.e., when the difference rises above about 1% meltwater fraction) as an indication of where to treat the derived values with caution.

[18] There are also bounds that we can impose on the meltwater fraction. It can be no less than zero, while equation (8) can be used to derive a theoretical upper bound, which occurs when the ocean temperature has been reduced to the freezing point ($\theta_{mix} = \theta_f$) and no further melting can occur. These limits are indicated in Figure 5. Profiles of derived meltwater fraction are plotted in Figure 6 for all the ice front stations. The bounds and the depths above which the numbers should be regarded as suspect are also indicated in Figure 6. At both ice fronts the melt concentration increases above a depth of about 400 m, approximately the maximum draft of the ice shelf. The distribution across the width of the ice shelf is relatively uniform with only a slight increase to the west (left in Figure 6, more apparent at the southern ice front), where we would expect to see the strongest outflows. Concentrations are higher at the northern ice front where they reach the theoretical upper bound. Formal error budgets are hard to quantify as most of the uncertainty arises from the assumption of linear mixing trends and the arbitrary choice of where the deviations from linearity become too great. However, the scatter of the data about the straight lines shown in Figure 5 suggests that in most cases the errors are around ±3 per mille or less. Before proceeding to make use of these data in combination with velocity estimates to calculate the net meltwater transport away from the ice shelf, we make use of other tracers to verify our estimates of meltwater fraction.

4. Discrete Bottle Data

[19] Other tracers that have commonly been used in the calculation of meltwater fraction are ratios of the stable
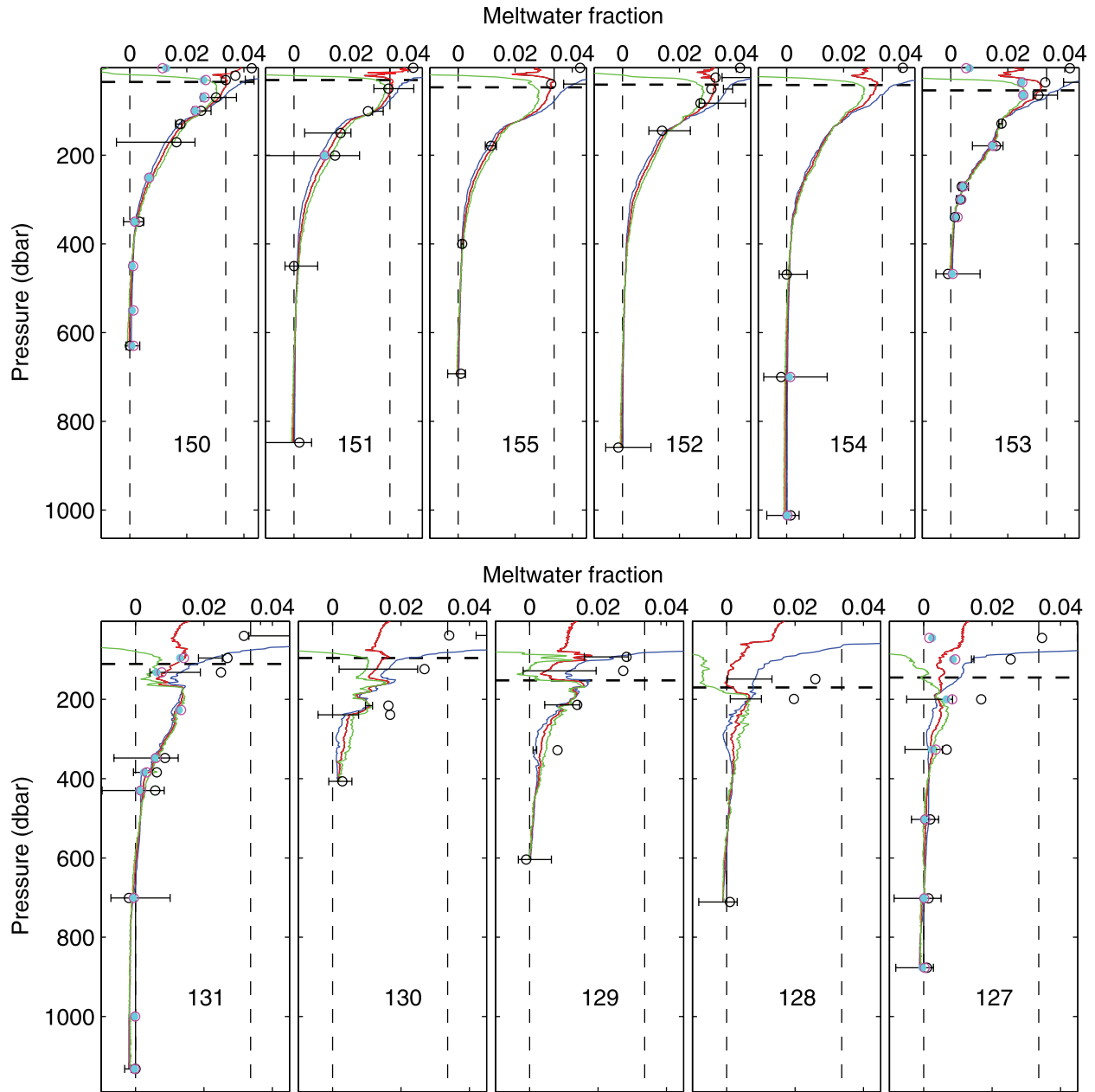
Figure 6. Profiles of meltwater fraction derived from data obtained at the (top) northern and (bottom) southern ice fronts. Continuous profiles were derived from θ/S (blue), O_2/S (red), and O_2/θ (green) data, while discrete values at bottle depths were derived from $\delta^{18}O/S$ and $\delta^{18}O/\theta$ (horizontal black lines), $\delta^{18}O$ alone (black circles), He/S (cyan dots), and Ne/S (magenta circles). The vertical dashed lines indicate zero and the theoretical upper bound, while the horizontal bold, dashed lines indicate the depth above which atmospheric interaction and additional freshwater sources disturb the meltwater signature.

isotopes of water and the concentrations of dissolved noble gases [*Weiss et al.*, 1979; *Schlosser*, 1986]. These can often give a relatively unambiguous indication of freshwater sources, but suffer from the disadvantage that measurements are only available from water samples collected at discrete depths. In polar regions precipitation is strongly depleted in the heavy isotopes of water, so it is a fairly simple matter to identify an admixture of meteoric water. However, distinguishing ice shelf melt from surface runoff or direct input of precipitation can be harder, particularly if the ice shelf, like

George VI, has a relatively low-lying, near-coastal catchment basin. The problems can be exacerbated by the poor signal-to-noise ratio in the data. The main advantage of the isotopic data is that they continue to provide a relatively clean signal of mixing processes, albeit complicated by additional water sources, in the surface layers, where temperature and dissolved gases undergo equilibration with the overlying atmosphere. Below the surface layer however, noble gas concentrations provide perhaps the cleanest signature of meltwater content, owing to their low solubility
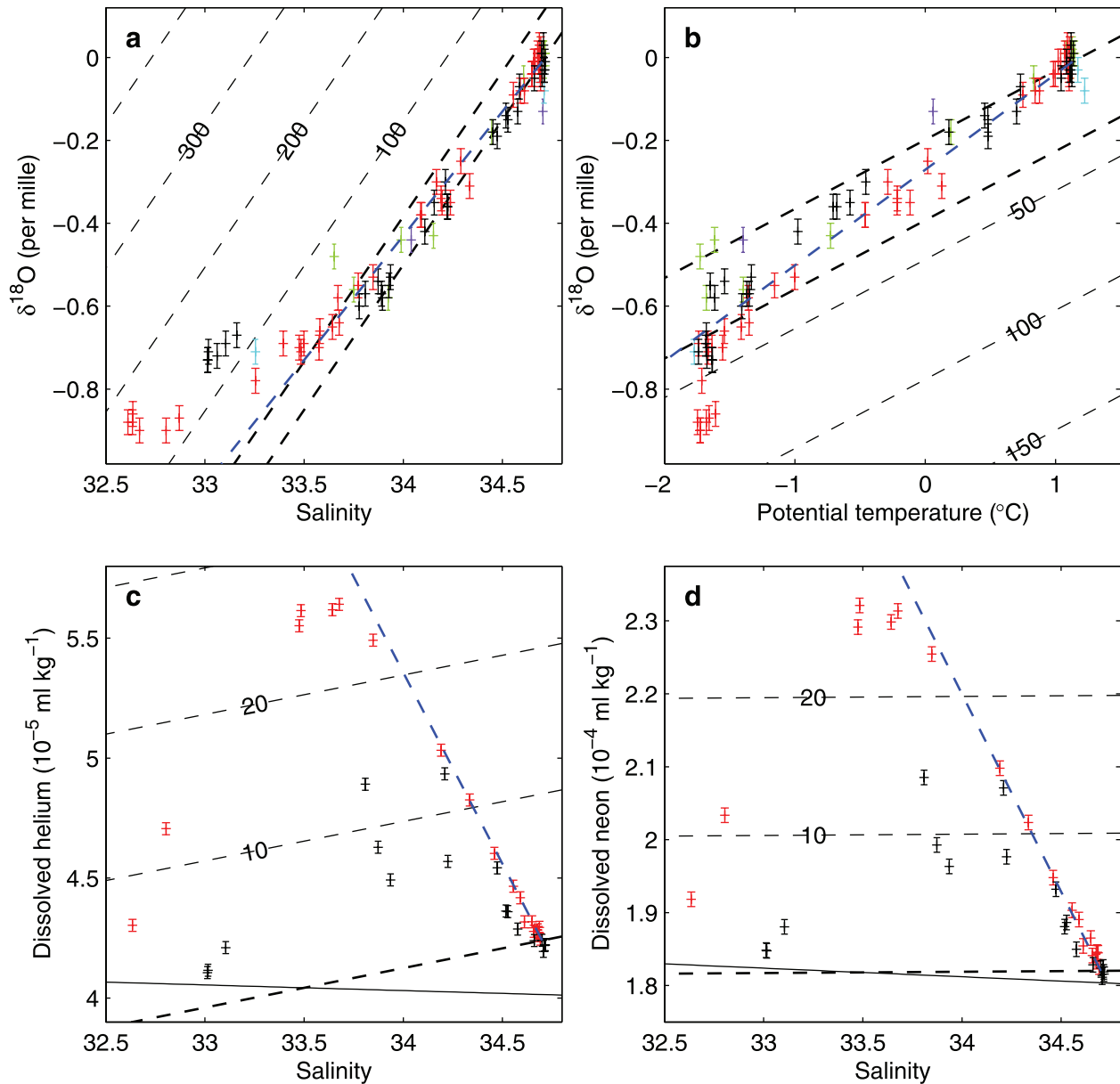
Figure 7. (a) The $\delta^{18}O/S$, (b) $\delta^{18}O/\theta$, (c) He/S, and (d) Ne/S data obtained at the stations marked in Figure 1. Color coding of the individual stations corresponds to that indicated in Figure 1. In all cases the numbered, light dashed lines are contours of meltwater fraction (per mille), while the bold dashed lines indicate the theoretical upper bound on the melt fraction and the CDW/WW trend used to define the zero melt fraction contour. The blue dashed lines indicate the CDW/meltwater mixing trends. The near-horizontal solid lines in Figures 7c and 7d indicate saturation concentrations for water at the surface freezing point.

in seawater and the small number of localized sources within the ocean [*Schlosser*, 1986; *Hohmann et al.*, 2002]. Bubble-mediated gas transfer at the ocean surface and, in the case of helium, input at mid-ocean ridges lead to a slight super-saturation at depth, but dissolution of air bubbles released from melting ice produces a signal many times greater. The result is that within our study area we find near-constant ambient concentrations and a unique helium/neon source in sub-surface melting ice, so that equations (2) and (4) are almost interchangeable.

[20] In Figure 7a we plot $\delta^{18}O$ against salinity. On first inspection these data show what appears to be a single mixing line, at least for salinities greater than 33.5. This is surprising given the clear distinction in the θ/S, O_2/θ and particularly the O_2/S plots between waters influenced by melt and those that comprise simple CDW/WW mixtures. Given this prior knowledge, it is just possible to define two analogous trends in the $\delta^{18}O/S$ data that form an envelope around the individual points (Figure 7a), although the spread of the two lines is less than the noise in the $\delta^{18}O$ data (around ±0.03 per mille, which alone leads to errors of

around ±9 per mille in the calculated meltwater fraction, irrespective of any nonlinearity in the trends) through most of the water column. Nonetheless, extrapolation of the meltwater mixing line to zero salinity gives an intercept of −20.8 per mille, the value estimated by *Potter et al.* [1984] for the mean $\delta^{18}O$ of the catchment basin. The ambient CDW/WW mixtures have more negative $\delta^{18}O$ values at any particular salinity than the CDW/meltwater mixtures. Surface runoff and local precipitation is presumably responsible for the freshest values lying to the left of the envelope, and the implication is that runoff and precipitation is less negative in $\delta^{18}O$ than ice shelf basal melt, as we would expect. However, when the formation of sea ice increases the salinity of the surface water to around 34, the $\delta^{18}O/S$ of the WW ends up to the right of the meltwater mixing line.

[21] *Jenkins* [1999] found that the $\delta^{18}O/\theta$ correlation was more useful in analyzing similar data from Pine Island Bay, and again in the case of these Bellingshausen Sea data we find that the separation of the melt-induced and ambient trends is greater on a $\delta^{18}O/\theta$ plot (Figure 7b). In fact we used the gradients of these two lines, multiplied by the gradients of the analogous lines in θ/S space, to define the two practically indistinguishable trends in $\delta^{18}O/S$ space. Again the calculation of meltwater fraction using the $\delta^{18}O/\theta$ data in equation (4) suffers from the fact that the small separation between the ambient and melt-induced trends means that errors in the $\delta^{18}O$ values cause relatively large errors in the meltwater fraction (around ±5 per mille), irrespective of any nonlinearity in the trends.

[22] Figure 6 indicates the spread in meltwater concentrations obtained from $\delta^{18}O/S$ and $\delta^{18}O/\theta$ data. There is considerable scatter and in the surface layers the derived values greatly exceed the theoretical maximum concentration. The compressed meltwater fraction scale, indicated by the closeness of the contours in Figures 7a and 7b, means that the different processes affecting the surface waters cause large errors in the derived meltwater content. Of course at the northern ice front, where we know the water column is a simple two-component CDW/meltwater mixture, we could use the $\delta^{18}O$ data independently, inserting the measured values directly into equation (2). This gives a more precise value for the meltwater content (around ±1.5 per mille if the only source of error is the $\delta^{18}O$ measurement) and corroborates our estimates based on O_2/S (Figure 6). In particular the magnitudes of the maxima in O_2/S-derived meltwater fraction just below the shallow surface layer agree well with the $\delta^{18}O$-derived numbers. However, a similar procedure applied at the southern ice front produces overestimates of meltwater fraction, because using $\delta^{18}O$ data alone it is impossible to distinguish between CDW/WW and CDW/meltwater mixtures.

[23] Within the study area noble gas concentrations were only measured at a few of the ice front sites, so we have insufficient data to define an ambient trend in He/S and Ne/S space (Figures 7c and 7d). However, *Hohmann et al.* [2002] presented all the NBP9402 helium data and showed that on a He/S plot the decline from super-saturation in the CDW to equilibrium concentrations at a salinity of around 33.5 is close to linear. We assume a similar ambient trend from CDW values to saturation concentrations at 33.5 in both He/S and Ne/S space, and in the latter case this leads to

an almost constant ambient Ne concentration (Figure 7d). We can define the meltwater mixing line on each plot using the air content of the ice implied by our dissolved oxygen measurements. Although gravitational fractionation within the firn will lead to depletions of these lighter gases relative to oxygen, the overall effect on the partial pressure should be less than 1% even for helium [*Craig et al.*, 1988]. The meltwater mixing lines derived in this manner fit very well with the observations, lending support to our choice of mixing line in O_2/S space. The utility of the noble gases as tracers of meltwater is evident from the wide separation of the ambient and melt-induced trends, giving an expanded meltwater fraction scale indicated by the widely spaced contours in Figures 7c and 7d. The errors in the individual measurements (around ±0.5% [*Hohmann et al.*, 2002]) lead to errors of around ±0.5 per mille or less in the calculated meltwater fractions. As on previous plots the northern ice front values lie very close to the CDW/meltwater mixing line. The drift away from this line at a salinity of around 33.5 is likely to be the result of gas loss through equilibration with the atmosphere, a process that has all but wiped out the meltwater signature at salinities of 33 and less. The derived meltwater fractions are consistent with our other estimates (Figure 6), except in the upper 50–100 m where all the signals are contaminated by interaction with the atmosphere. Although the noble gas data provide the most precise point measurements, we consider the overall best estimate of meltwater fraction to be that based on O_2/S, because the continuous profiles at every station enable us to define the structure and extent of even small-scale meltwater features.

5. Geostrophic Velocities

[24] We now wish to calculate transports of meltwater into and out of the cavity beneath George VI Ice Shelf. Since we have no direct observations of currents contemporaneous with our CTD data, we must estimate them by calculating water densities and assuming that the flows are in hydrostatic and geostrophic balance:

$$f\frac{\partial v}{\partial P} = -\frac{\partial \alpha}{\partial x}\bigg|_P, \qquad (10)$$

where f is the Coriolis parameter, v is velocity perpendicular to the CTD section, P is pressure, α is specific volume, x is the horizontal axis and the derivative is taken along isobaric surfaces. By integrating this equation with respect to pressure we can calculate the velocity on any pressure surface relative to that at a reference pressure:

$$v(P) = v(P_{ref}) + \frac{1}{f}\frac{\partial}{\partial \chi}\left(\int_P^{P_{ref}} \alpha\, dp\right)\bigg|_P. \qquad (11)$$

We refer to the first term on the right-hand side of equation (11) as the reference velocity and the second term as the relative velocity. The horizontal derivative is evaluated between CTD stations and the derived velocities are then applied to the entire area between the stations. There are several problems to be overcome before we can estimate full-depth velocity profiles along our sections: defining the
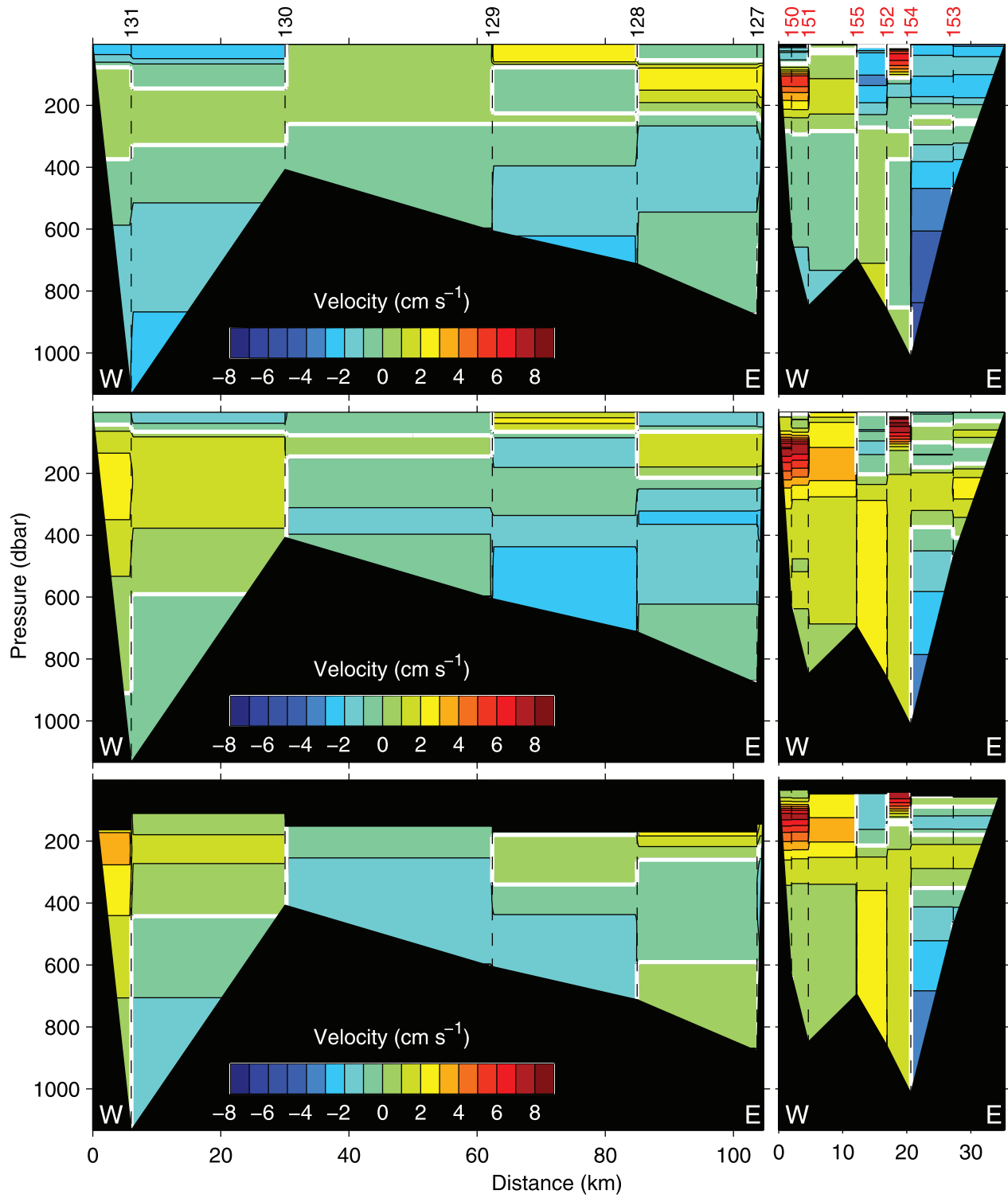
Figure 8. (top) Initial and (middle and bottom) final velocities calculated at the (left) southern and (right) northern ice fronts. Positive values indicate flow out of the cavity (into the page), and the bold white line corresponds to zero velocity. The initial velocities were set to have a level of zero motion along the 5 per mille meltwater fraction contour. The final velocities represent a minimal adjustment to the initial values that will permit overall balanced tracer budgets over the full water column (middle) and over the partial water column where the meltwater fraction calculations are unaffected by atmospheric interaction (bottom). In the latter case the part of the water column excluded from the consideration is shaded black.

reference velocities, evaluating the relative velocities below the level of the greatest common pressure on adjacent CTD stations, and evaluating transports between the section ends and the coast.

[25] The latter problems require extrapolation of our observations into the unsampled regions. There are a number of ways of doing this and the choice is arbitrary. For vertical extrapolation of temperature and salinity beyond the greatest common pressure we require that the resulting density structure gives us a predetermined simple velocity structure in the lower part of the water column. The velocity structure is derived from the vertical shear evaluated at the greatest common pressure. From this point we either keep the vertical shear constant down to the seabed, allow it to decrease linearly to zero at the seabed, or set it to zero everywhere so that the velocity stays constant from the greatest common pressure down to the seabed. We adopt the second of these as standard, but try all three options to see how sensitive our final results are to this rather arbitrary extrapolation. Other tracers are extrapolated in the same way as temperature and salinity. Since earlier observations [*Potter et al.*, 1988] indicate that outflows can be concentrated in narrow coastal jets we also wish to extrapolate our data into the regions between the ends of our sections and the coast. To do this we simply assume that the isobaric property gradients observed between the outer station pairs continue unaltered to the coast. This procedure makes the relative velocity in the unsampled regions the same as that calculated between the outer station pairs. The alternative of holding the properties constant from the outer station to the coast, thus making the relative velocity zero, has also been tried, as has the strategy of terminating the sections at the outer stations, so that no lateral extrapolation is required.

[26] To tackle the first problem, that of the reference velocity, we use our estimates of the meltwater concentration as a guide. We assume that waters with a significant meltwater content are flowing out of the cavity, while those with near zero concentrations of melt are flowing in. The divide between near zero and significant is arbitrarily set at a concentration of 5 per mille. Since the velocity is applied to the whole area between stations we take the mean of the meltwater concentration at adjacent stations and select the pressure at which this falls below the threshold. We set the velocity at this pressure to zero. The results are shown in Figure 8. As a sensitivity test we also try levels of zero motion defined at the sea surface and the seabed.

6. Constraints on the Velocities

[27] In principle we now have enough information to calculate the transport of meltwater away from the ice shelf. However, our choice of a zero velocity level is little more than an educated guess, and does not always guarantee that the upper part of the water column is flowing out of the cavity and the lower part in (Figure 8). Indeed, since there are other ice shelves in the region, having some meltwater flowing into the cavity is perfectly reasonable. Hence there is scope to make minor adjustments to the reference velocities and in so doing ensure that the overall circulation we derive satisfies certain global constraints such as conservation of mass and tracers within the cavity. To do this we apply the well-used techniques of *Wunsch* [1978].

[28] Since our CTD sections effectively close off the cavity, we know that the total mass transport across them must fit with the constraint:

$$\sum_{j=1}^{n+4} (M_{out} - M_{in})_j = M_{melt}, \tag{12}$$

where M is mass and the summation runs over n individual station pairs plus four gaps between the section ends and the coast. Similarly total transport of tracers must satisfy:

$$\sum_{j=1}^{n+4} \left[(M\chi)_{out} - (M\chi)_{in} \right]_j = M_{melt}\chi_{melt}. \tag{13}$$

Our analyses described in the preceding two sections yielded values of χ_{melt} (the zero salinity endpoint of the CDW/meltwater mixing lines), so the only unknown in equation (13) is the total mass of meltwater transported across the sections. Combining equations (12) and (13) we can eliminate the unknown meltwater transport:

$$\sum_{j=1}^{n+4} \left\{ [M(\chi - \chi_{melt})]_{out} - [M(\chi - \chi_{melt})]_{in} \right\}_j = 0, \tag{14}$$

In formulating this balance we are assuming that χ_{melt} is constant over the ice shelf. The near linearity of the CDW/meltwater mixing lines discussed earlier supports this assumption, and as a consequence implies that meltwater drainage through and refreezing at the base of the ice shelf are negligible. The absence of a significant quantity of water at or near the freezing point in situ is consistent with negligible refreezing, and observations suggest that both meltwater drainage and refreezing occur only in isolated regions [*Reynolds*, 1981; *Pedley et al.*, 1988]. The transport between each station pair can be obtained from an integration of the velocity profile with respect to pressure:

$$\left\{ [M(\chi - \chi_{melt})]_{out} - [M(\chi - \chi_{melt})]_{in} \right\}_j$$
$$= \frac{1}{g} \left\{ \int_{P_{bot}}^{P_{top}} v(p)[\chi(p) - \chi_{melt}]\Delta x(p)dp \right\}_j, \tag{15}$$

where Δx is the width of the gate; constant with pressure except in the unsampled regions where we assume it decreases linearly to zero (i.e., the areas between adjacent stations are made trapezoidal in shape through the addition of a bottom triangle). Similarly we assume a triangular cross-section for the regions between the end stations of each section and the coast.

[29] The velocity in equation (15) comprises two parts, the known relative velocity, v_{rel}, which we obtained from the measured specific volume profiles, and the unknown reference velocity, v_{ref}. Equation (14) thus contains $n+4$ unknown reference velocities, and we have m such equations, one for each observed tracer, that can be written in matrix form as:

$$\mathbf{Av} + \mathbf{b} = \mathbf{0}, \tag{16}$$

Table 1a. Total and Meltwater Transports Across the Northern and Southern Ice Fronts Calculated by Inversion of the Tracer Budget Equations Integrated Over the Full Water Column

| | Southern Ice Front Transport | | | | | | Northern Ice Front Transport | | | | | | |
| | Total (Sv) | | | Melt (km^3 a^{-1}) | | | Total (Sv) | | | Melt (km^3 a^{-1}) | | | |
Model	In	Out	Net	In	Out	Net	In	Out	Net	In	Out	Net	Overall Transport (km^3 a^{-1})
Standard	−0.506	0.239	−0.267	−50.9	66.2	15.3	−0.060	0.330	0.270	−12.0	113.2	101.1	119.0
Uniform triangles	−0.523	0.301	−0.222	−78.6	72.4	−6.1	−0.069	0.293	0.224	−13.0	98.0	85.0	80.0
No triangles	−0.513	0.284	−0.229	−75.3	68.8	−6.5	−0.064	0.295	0.231	−11.4	94.6	83.2	77.8
Constant shear	−0.530	0.257	−0.273	−54.8	70.3	15.5	−0.065	0.342	0.277	−11.6	115.1	103.5	122.8
No shear	−0.474	0.231	−0.242	−45.8	60.7	14.9	−0.047	0.292	0.246	−14.5	106.6	92.2	107.8
Surface reference	−0.652	0.475	−0.178	−68.5	99.3	30.8	−0.144	0.324	0.181	−36.1	121.4	85.4	116.0
Seabed reference	−0.558	0.303	−0.255	−75.8	83.9	8.1	−0.047	0.305	0.258	−31.5	130.6	99.1	109.0
Gate area weighting	−0.477	0.148	−0.329	−44.5	44.4	−0.1	−0.050	0.383	0.333	−9.0	125.2	116.2	120.3
No weighting	−0.536	0.266	−0.270	−47.8	73.0	25.2	−0.057	0.331	0.274	−17.8	111.6	93.8	121.5
Mean	−0.530	0.278	−0.252	−60.2	71.0	10.8	−0.067	0.322	0.255	−17.4	112.9	95.5	108.2
Standard deviation	0.053	0.088	0.042	14.2	15.1	13.1	0.030	0.030	0.042	9.7	11.9	10.7	17.4

where:

$$A_{ij} = \frac{1}{g} \left\{ \int_{P_{bot}}^{P_{top}} [\chi_i(p) - \chi_{melt}] \Delta x(p) dp \right\}_j, \quad (17)$$

$$b_i = \frac{1}{g} \sum_{j=1}^{n+4} \left\{ \int_{P_{bot}}^{P_{top}} v_{rel}(p)[\chi_i(p) - \chi_{melt}] \Delta x(p) dp \right\}_j, \quad (18)$$

$$v_j = (v_{ref})_j. \quad (19)$$

In practice we have fewer equations than unknowns ($m < n+4$), so equation (16) has no unique solution. The procedure described by *Wunsch* [1978] allows us to choose from the infinite number of possible solutions the one that has the smallest vector, **v**. Since our initial estimate for the circulation set the reference velocities to zero, this particular solution represents the smallest possible adjustment to our initial guess that will allow us to satisfy the constraints imposed by equation (14). In formulating equation (16) we use the three tracers, potential temperature, salinity and dissolved oxygen, for which we have full-depth continuous profiles. The integrals in equations (17) and (18) could be performed either over the entire depth of the water column or only over that part where we are confident that we can relate variations in temperature, salinity and dissolved oxygen to the addition of meltwater (i.e., between the seabed and the horizontal dashed

lines in Figure 6). We adopt both strategies here, since neither is problem-free. Using the full water column we include regions where processes other than melting have influenced the water properties (so equation (13) is not strictly valid), while using the partial water column we exclude regions where we know that meltwater must exit the sub-ice cavity.

[30] *Wunsch* [1978] discusses the impact of weighting the columns of **A** on the structure of the minimum length solution for **v**. If the CTD stations are unevenly spaced the total transport can be adjusted with smaller v_j, if those adjustments are applied to widely spaced station pairs. The minimum length solution thus naturally favors regions that are more sparsely sampled, and this could be undesirable. This bias can be removed by weighting the columns of **A** by the inverse of the area enclosed by each station pair. The minimum length solution then becomes (*Wunsch*, 1978):

$$\mathbf{v} = \mathbf{W}^{-1}\mathbf{A}^T(\mathbf{A}\mathbf{W}^{-1}\mathbf{A}^T)^{-1}(-\mathbf{b}) \quad (20)$$

where **W** is a diagonal matrix with elements:

$$W_{jj} = \frac{1}{g} \left\{ \int_{P_{bot}}^{P_{top}} \Delta x(p) dp \right\}_j. \quad (21)$$

Note that our weights formally include the water density as a multiplicative factor, but this varies little between station pairs. We actually modify the weight matrix further to avoid the possibility that in treating each station pair equally we

Table 1b. Total and Meltwater Transports Across the Northern and Southern Ice Fronts Calculated by Inversion of the Tracer Budget Equations Integrated Over the Partial Water Column

| | Southern Ice Front Transport | | | | | | Northern Ice Front Transport | | | | | | |
| | Total (Sv) | | | Melt (km^3 a^{-1}) | | | Total (Sv) | | | Melt (km^3 a^{-1}) | | | |
Model	In	Out	Net	In	Out	Net	In	Out	Net	In	Out	Net	Overall Transport (km^3 a^{-1})
Standard	−0.312	0.146	−0.165	−20.8	33.0	12.2	−0.076	0.243	0.167	−13.8	76.8	62.9	77.6
Uniform triangles	−0.298	0.103	−0.195	−16.2	18.8	2.6	−0.071	0.268	0.197	−10.6	84.3	73.7	79.4
No triangles	−0.293	0.103	−0.190	−19.1	19.4	0.3	−0.065	0.256	0.192	−9.1	73.1	63.9	67.1
Constant shear	−0.335	0.162	−0.174	−22.9	37.0	14.1	−0.078	0.254	0.176	−12.6	79.2	66.6	84.5
No shear	−0.243	0.111	−0.132	−14.7	22.7	8.0	−0.072	0.205	0.133	−19.3	69.0	49.8	58.2
Surface reference	−0.454	0.232	−0.223	−26.7	50.1	23.4	−0.100	0.326	0.226	−19.6	108.1	88.5	115.0
Seabed reference	−0.363	0.152	−0.211	−18.0	33.9	15.9	−0.053	0.267	0.214	−25.5	102.4	76.9	96.6
Gate area weighting	−0.306	0.089	−0.217	−13.4	24.4	11.0	−0.059	0.278	0.220	−9.5	85.1	75.6	90.0
No weighting	−0.312	0.130	−0.182	−22.8	28.2	5.4	−0.079	0.264	0.184	−19.3	80.1	60.8	69.0
Mean	−0.324	0.136	−0.188	−19.4	29.7	10.3	−0.073	0.262	0.190	−15.5	84.2	68.7	81.9
Standard deviation	0.058	0.044	0.029	4.3	10.0	7.2	0.014	0.032	0.029	5.7	13.1	11.3	17.2

could introduce a slight bias toward the better sampled northern ice front section. To account for this we divide each element of the weight matrix by the sum of the weights applied to each section. The trace of **W** is then equal to two and the individual elements are the fractional contribution of each station pair to the total area of the appropriate section. We adopt this latter strategy as standard but discuss solutions with **W** as defined in equation (21) and with no weighting (i.e., **W** is the identity matrix).

7. Results

[31] The velocity sections that result from adding the reference velocities calculated from equation (20) to the relative velocities derived from equation (11) are shown in the lower two panels of Figure 8. In one of these we have integrated velocity and tracer concentration over the entire water column, while in the other we have excluded the upper parts where processes other than melting impact the concentrations. We find that in both cases the tracer budgets (equation (14)) can be satisfied with relatively small reference velocities, less that 2.5 cm s^{-1} in magnitude, applied at the reference levels. The solutions appear physically reasonable in that the strongest outflows appear high in the water column against the western coast, while the inflows are generally strongest at depth and in the east. The overall structure found for the northern ice front section shows many of the features found by *Potter et al.* [1988], with the exception of the weak inflow, present also in our initial velocity assumptions, they postulated everywhere below about 400 m. The velocities calculated by *Potter et al.* [1988] provided a near balance between inflow and outflow at the northern ice front. In contrast we find that the outflow at the north (0.33/0.24 Sv, Full/Partial water column, Standard Model, Tables 1a and 1b) greatly exceeds the inflow there (0.06/0.08 Sv), 70–80% of it being supplied by a throughflow from the south, where only about half of the 0.51/0.31 Sv inflow re-emerges. Such a net throughflow of 0.27/0.17 Sv from south to north in the sound is consistent with our inference above that the northern ice front is dominated by CDW sourced from the south and that a particularly strong meltwater signature can be traced out into Marguerite Bay.

[32] Now combining the results in Figure 8 with those in Figure 6 we can calculate the transport of meltwater into and out of the cavity. At the southern ice front the derived meltwater outflow of 66/33 km^3 a^{-1} is partially offset by an inflow of 51/21 km^3 a^{-1}. At the northern ice front only 12/14 km^3 a^{-1} flow into the cavity while 113/77 km^3 a^{-1} flow out. The net production of meltwater within the cavity then totals 116/75 km^3 a^{-1}. This last quantity can also be estimated from the net flow out of the cavity (equation (12)), which in this case is 119/78 km^3 a^{-1}. The small difference between the calculated net volume transport away from the cavity and the total meltwater transport across both ice fronts is an indication of the internal consistency of the results. Drawn from the 25,000 km^2 area of the ice shelf, the latter numbers suggest a mean melt rate of 4.8/3.1 m a^{-1}.

[33] The above results are summarized in Tables 1a and 1b, as the "Standard" model covering the "Full" (Table 1a)

or "Partial" (Table 1b) water depth. The remainder of Tables 1a and 1b shows how sensitive these results are to the changes in the model setup that have been discussed in previous sections. In all cases the changes are made individually to the "Standard" setup. We have tried extrapolating beyond the ends of the section assuming no property gradients along isobaric surfaces ("Uniform triangles"), terminating the sections at the outer CTD stations ("No triangles"), filling the unsampled areas between stations of unequal depth by an extrapolation that gives constant shear ("Constant shear") or constant velocity ("No shear") in this region, setting the reference level where the velocity is initially zero at the surface ("Surface reference") and at the seabed ("Seabed reference"), applying column weighting as defined in equation (21) ("Gate area weighting") and using no column weighting ("No weighting"). The total range in numbers that we obtain does not greatly exceed the difference quoted above for the "Full/Partial Standard" model, and the general structure of the inflows and outflows shown in Figure 8 does not change. Robust features of the results include a south to north throughflow equal to about half the size of the southern inflow and a net meltwater production in the south that ranges from near zero to a maximum of about 25% of the total production.

[34] Formal errors in the budgets are quite difficult to estimate, because most of the uncertainty arises from the assumptions we made in calculating the velocity profiles: that the flow is adequately sampled, steady and geostrophic. In particular, the summary statistics at the bottom of Tables 1a and 1b should not be interpreted in their conventional sense as best estimates of the true value and precision. They are only provided as convenient summaries of the spread in the results.

8. Discussion

[35] *Potter and Paren* [1985] estimated an equilibrium melt rate of 2.1 m a^{-1} for the ice shelf as a whole, while time series data at ERS altimeter crossover points indicates that the ice shelf is thinning at a spatially variable rate of 1–3 m a^{-1} (A. Shepherd, personal communication, 2007). Together these suggest an average net melt rate of around 4 m a^{-1}. *Corr et al.* [2002] measured a melt rate of 2.8 m a^{-1} over a twelve-day period in December 2000 at one point on the southern part of the ice shelf. Thus our derived melt rates, which range from 2.3 to 4.9 m a^{-1} (Tables 1a and 1b), are broadly consistent with these two independent estimates of the actual melt rate, and indicate that the ice shelf is in a state of negative disequilibrium. Note that our estimate is averaged over the entire ice shelf, and there is considerable spatial variability in the melt rate [*Bishop and Walton*, 1981]. Also, our estimate is a one week snapshot, and there could be temporal variability in the melt rate associated with intermittent delivery of CDW to the continental shelf [*Klinck et al.*, 2004].

[36] Perhaps the most unexpected aspect of our results is the low (sometimes negative) net meltwater flux across the southern ice front in most of the solutions. If we assume that the ridge of maximum ice thickness acts as a meltwatershed, then 2/5 of the basal area supplies melt to the southern outflows and 3/5 to the northern outflows. There is no obvious reason to expect dramatically lower melt rates in

the south. *Potter and Paren* [1985] estimated similar equilibrium melt rates for north and south, and the measurement of *Corr et al.* [2002] was made just on the southern side of the region of maximum ice thickness. The apparently poorer results for the southern ice front may be because some of the melt signature is lost by upwelling and mixing into the relatively deep surface mixed layer (Figure 6). At the northern ice front, at the time of the observations, the meltwater was upwelling beneath a fast ice cover, which protected it from the atmosphere and preserved the meltwater signature until the water was sampled directly at the fast ice edge. The southern ice front section also suffers from poorer horizontal resolution, so some of the details of the outflows could have been missed. Our sampling would also have missed any outflows that pass to the south of Spaatz Island (Figure 1). However, some of the meltwater generated in the south could be carried with the general flow through to the northern ice front. Another possibility is that a portion of the large meltwater inflow at the southern ice front, which may have come from Bach and Wilkins ice shelves (Figure 1) but might also include meltwater that has recirculated from the also substantial southern outflow, could be carried through the cavity to exit at the northern ice front. If this were the case our estimates of net meltwater production in the south and north would have to be adjusted up and down by an equivalent amount. For example, if meltwater were uniformly distributed over the southern inflow, roughly half would exit in the north, and the net meltwater production would then be split approximately 35/65 between south and north.

[37] Observations in the region of Marguerite Bay [*Klinck et al.*, 2004] suggest a flow toward the south and west on the outer shelf, with cyclonic circulation around the Bay. If the general southwestward flow carries on along the outer shelf we might expect similar cyclonic circulation around Ronne Entrance, consistent with waters at the southern George VI Ice Front having picked up some melt from the ice shelves to the north and east. Our observed through-flow within George VI Sound would then represent a partial recirculation of waters back to Marguerite Bay. Such a pattern of circulation is analogous to that set up beneath some of the larger ice shelves. For example a westward coastal current, driven by southerly winds and local freshening, follows Filchner-Ronne Ice Front, while anti-cyclonic circulation beneath the ice shelf carries water back to the east [*Foldvik et al.*, 2001; *Nicholls et al.*, 2001]. However, there are also differences in that the flow beneath Filchner-Ronne Ice Shelf is primarily driven by the formation of dense shelf waters during winter at the western end of the ice front. In the case of George VI Ice Shelf there should be minimal seasonal buoyancy forcing on the deep circulation and although we observe higher densities at the southern ice front the north-south difference is small. The pressure gradient driving the throughflow may be set up by surface wind-forcing, while the buoyancy imparted by the melting ice shelf could be a significant driver of the upper water column outflows at both ice fronts, as hypothesized by *Potter and Paren* [1985].

[38] Although we have focused on the meltwater content of the upper water column outflows, the fraction of meltwater rises to a maximum of only around 3%, so the outflows consist primarily of CDW. However, the small admixture of meltwater is sufficient to lower the density of the CDW/meltwater mixture to and below that of WW, defined as having a salinity of 34 and a potential temperature equal to the surface freezing point. The outflows thus represent a flux of slightly modified CDW, with associated high temperature, low dissolved oxygen and high nutrient concentrations, to the surface layers of Marguerite Bay and Ronne Entrance. For the standard (full/partial) model the fluxes of modified CDW into the mixed layer and the associated heat fluxes are quantified in Table 2. The net outflow from both ice fronts totals about 0.1 Sv and carries a heat flux of around 200 GW. Although this represents only about one quarter of the heat that was extracted from the CDW to melt ice from the ice shelf base, it is equivalent to a vertical heat flux of 8 W m^{-2} over that area. *Howard et al.* [2004] estimate that vertical mixing in the main pycnocline supplies an average of <2 W m^{-2} to the mixed layer in Marguerite Bay, giving a total vertical heat flux of <150 GW over their 75,000 km^2 survey area. The heat flux at the northern ice front of George VI Ice Shelf is thus of comparable magnitude, and comes with a supply of nutrients [*Giulivi and Jacobs*, 1997], which will have some significance for the Bay ecosystems. *Howard et al.* [2004] suggested that wind-driven coastal upwelling could be a major contributor to the upward flux of CDW properties. Our study highlights the buoyancy imparted by melting ice as an important additional driver of upwelling. George VI Ice Shelf represents only about 50% by area of the ice shelf cover over the western Bellingshausen Sea continental shelf (Figure 1). Similar processes must operate beneath Wilkins, Bach and Stange ice shelves, and together they could drive upwelling of an additional ~0.1 Sv of CDW, although the impacts would be less geographically focused.

[39] Based on these brief snapshots of conditions near each ice front, we cannot address temporal variability in the described flows. Changes in the local wind-forcing could impart relatively high frequency variability to the system, while the growth and decay of sea ice will seasonally modulate the degree to which the wind stress is transmitted to the ocean. Assuming that buoyancy forcing associated with sea ice growth and melt is confined to levels in the water column that are dominated by outflow, it should not greatly influence circulation beneath the ice shelf. Temporal variability in the inflow properties could be caused by the intermittent supply of CDW to the shelf. *Klinck et al.* [2004] suggest that 4–6 intrusions per year occur within their study area centered on Marguerite Bay, with the locations of the inflows being topographically controlled, and the timing associated with variability in the Antarctic Circumpolar Current, the southern boundary of which runs along the continental slope in this region. Marguerite Bay CDW appears to play a minor role in the circulation beneath George VI Ice Shelf, at least at the time of the observations reported here, and it remains to be determined whether CDW is intermittently supplied to Ronne Entrance, and whether that leads to variability in the mean temperature and mean melt rate beneath George VI Ice Shelf.

9. Summary and Conclusions

[40] We have discussed the results of near synchronous surveys of the oceanographic conditions at the northern and

Table 2. Transport of Modified CDW at Densities Less Than or Equal to That of WW

Standard Model, Full or Partial	Southern Ice Front			Northern Ice Front		
	In	Out	Net	In	Out	Net
	Modified CDW Volume Transport (Sv)					
Full	−0.067	0.099	0.032	−0.009	0.067	0.059
Partial	−0.057	0.125	0.067	−0.017	0.056	0.039
	Modified CDW Heat Transport (GW)					
Full	−71.9	150.8	78.9	−17.9	148.3	130.4
Partial	−54.2	159.2	104.9	−31.6	121.4	89.8

southern ice fronts of George VI Ice Shelf. Both are dominated by CDW, which flows beneath the ice shelf and drives basal melting. We have analyzed various combinations of conservative tracers to derive consistent values for the concentration of meltwater present in the water column. The tracer we have relied most heavily on is one that is not commonly used for this purpose, and that in many situations cannot be regarded as conservative. However, in this environment, dissolved oxygen concentrations allow us to distinguish CDW that has been freshened and cooled by melting beneath the ice shelf, a process that adds only a small amount of dissolved oxygen, from CDW that has been freshened and cooled by mixing with oxygen-saturated surface waters. At least three water masses contribute to properties observed near the ice shelf, so we have used combinations of two tracers to calculate meltwater concentrations [*Jenkins*, 1999]. We have shown how the use of multiple combinations of tracers can help resolve ambiguities in the individual data sets. For example, use of the δ^{18}O/S diagram (Figure 7a) alone would have suggested that both ice fronts could be characterized by the same simple CDW/meltwater mixing line, and would have led to over-estimates of meltwater concentration in the south. Although the low concentrations in all inflowing waters mean that noble gases provide the most precise measure of the added meltwater fraction, the inevitable sparsity of the sampling entails an over-dependence on spatial extrapolation, were these data to be used alone. All the dissolved gases undergo equilibrium with the atmosphere once the water is in the surface layers, and the potential temperature is modified by surface heat fluxes. Thus, most of the records of sub-surface melting are lost in the surface mixed layer, although the process is slowed by presence of a sea ice cover. Only salinity and the stable isotope ratios retain the melt signature, but they are modified by multiple additional freshwater sources as well as the growth and decay of sea ice, making it hard, if not impossible, to extract quantitative information on near-surface meltwater concentrations. However, below the surface layers our calculations show melt at both ice fronts above the level of the maximum ice shelf draft, although concentrations are higher at the northern ice front, where they reach the theoretical maximum (i.e., the water has been cooled from its initial temperature to the freezing point by interaction with the ice shelf). The signature of similarly high concentrations could have been damped at the southern ice front, through upwelling of the outflowing water and its incorporation into a deeper surface mixed layer. However, the persistence of a strong melt signature extending well into Marguerite Bay, and the

weaker inflow signal from the north are genuine features and not sampling artifacts.

[41] We have used the tracers for which we have continuous profiles to constrain geostrophic velocity estimates and derive the overall circulation and net melt rate. Half the 0.3−0.5 Sv inflow in the south re-emerges there and half continues along the sound to the north, where there is only a minor addition from the 0.07 Sv inflow. Net meltwater transport ($\sim$0.003 Sv) barely rises above the noise level of the calculations and is influenced to an unknown degree by temporal variability in the shelf water properties. Nevertheless, our calculated mean melt rate exceeds the 2.1 m a^{-1} equilibrium value of *Potter and Paren* [1985] by a factor of 50−150% and is consistent with other observations of thinning and retreat of the ice shelf. Much of the meltwater produced beneath the ice shelf appears to be carried northward by the mean flow through the sound, emerging in southern Marguerite Bay. Since the outflows comprise >97% CDW, the coincident upwelling has a significant impact on the mid- and upper water column properties, making a substantial contribution to vertical heat and nutrient fluxes.

[42] The role played by the ice shelf in promoting the exchange of heat between CDW and the surface mixed layer is intriguing in several respects. Upwelling of CDW beneath the ice shelf is presumably a year-round phenomenon, and the associated heat flux must limit the growth of sea ice over the Bellingshausen Sea continental shelf. The associated weak salt flux precludes the formation of saline shelf waters, which in turn is a factor permitting the inflow of almost unmodified CDW to the deepest regions of the continental shelf. If the on-shelf presence of CDW is maintained partly by the rapid melting fuelled by its heat content, then substantial ice shelf retreat could result in overall cooling of shelf waters. This admittedly speculative link between shelf water properties and ice shelf extent raises the possibility of self-sustained cycles of ice shelf advance and retreat, with consequent ecosystem impacts and sediment histories.

References

Arctowski, H., H. R. Mill (1908), Relations thermiques: Rapport sur les observations thermométriques faites aux stations de sondages, in *Expedition Antarctique Belge: Résultats du Voyage du S. Y. Belgica en 1897−1898−1899, Rapp. Sci*, vol. 5, 36 pp., J.-E. Buschmann, Anvers, Belgium.

Bentley, M. J., D. A. Hodgson, D. E. Sugden, S. J. Roberts, J. A. Smith, M. J. Leng, and C. Bryant (2005), Early Holocene retreat of the George VI Ice Shelf, Antarctic Peninsula, *Geology*, *33*, 173–176, doi:10.1130/G21203.1.

Bishop, J. F., and J. L. W. Walton (1981), Bottom melting under George VI Ice Shelf, Antarctica, *J. Glaciol.*, *27*, 429–447.

Corr, H. F. J., A. Jenkins, K. W. Nicholls, and C. S. M. Doake (2002), Precise measurement of changes in ice-shelf thickness by phase-sensitive radar to determine basal melt rates, *Geophys. Res. Lett.*, *29*(8), 1232, doi:10.1029/2001GL014618.

Craig, H., Y. Horibe, and T. Sowers (1988), Gravitational separation of gases and isotopes in polar ice caps, *Science*, *242*, 1675–1678, doi:10.1126/science.242.4886.1675.

Doake, C. S. M., and D. G. Vaughan (1991), Rapid disintegration of the Wordie Ice Shelf in response to atmospheric warming, *Nature*, *350*, 328–330, doi:10.1038/350328a0.

Foldvik, A., T. Gammelsrød, E. Nygaard, and S. Østerhus (2001), Current measurements near Ronne Ice Shelf: Implications for circulation and melting, *J. Geophys. Res.*, *106*, 4463–4477, doi:10.1029/2000JC000217.

Giulivi, C. F., and S. S. Jacobs (1997), Oceanographic data in the Amundsen and Bellingshausen Seas, *N. B. Palmer* Cruise 9402, Feb–Mar 1994, *Tech. Rep. LDEO-97–3*, 330 pp., Lamont-Doherty Earth Obs., Palisades, N. Y.

Hellmer, H. H., S. S. Jacobs, and A. Jenkins (1998), Oceanic erosion of a floating Antarctic glacier in the Amundsen Sea, in *Ocean, Ice, and Atmosphere: Interactions at the Antarctic Continental Margin, Antarct. Res. Ser.*, vol. 75, edited by S. S. Jacobs and R. F. Weiss, pp. 83–99, AGU, Washington, D. C.

Hjort, C., M. J. Bentley, and Ó. Ingólfsson (2001), Holocene and pre-Holocene temporary disappearance of the George VI Ice Shelf, Antarctic Peninsula, *Antarct. Sci.*, *13*, 296–301, doi:10.1017/S0954102001000426.

Hohmann, R., P. Schlosser, S. Jacobs, A. Ludin, and R. Weppernig (2002), Excess helium and neon in the southeast Pacific: Tracers for glacial melt-water, *J. Geophys. Res.*, *107*(C11), 3198, doi:10.1029/2000JC000378.

Howard, S. L., J. Hyatt, and L. Padman (2004), Mixing in the pycnocline over the western Antarctic Peninsula shelf during Southern Ocean GLOBEC, *Deep Sea Res., Part II*, *51*, 1965–1979, doi:10.1016/j.dsr2.2004.08.002.

Jacobs, S. S., H. H. Hellmer, and A. Jenkins (1996), Antarctic ice sheet melting in the Southeast Pacific, *Geophys. Res. Lett.*, *23*(9), 957–960, doi:10.1029/96GL00723.

Jenkins, A. (1999), The impact of melting ice on ocean waters, *J. Phys. Oceanogr.*, *29*, 2370–2381, doi:10.1175/1520-0485(1999)029<2370:TIOMIO>2.0.CO;2.

Klinck, J. M., E. E. Hofmann, R. C. Beardsley, B. Salihoglu, and S. Howard (2004), Water mass properties and circulation on the west Antarctic Peninsula continental shelf in the austral fall and winter 2001, *Deep Sea Res., Part II*, *51*, 1925–1946, doi:10.1016/j.dsr2.2004.08.001.

Lennon, P. W., J. Loynes, J. G. Paren, and J. R. Potter (1982), Oceanographic observations from George VI Ice Shelf, Antarctic Peninsula, *Ann. Glaciol.*, *3*, 178–183.

Lucchitta, B. K., and C. E. Rosanova (1998), Retreat of northern margins of George VI and Wilkins ice shelves, Antarctic Peninsula, *Ann. Glaciol.*, *27*, 41–46.

Martinerie, P., D. Raynaud, D. M. Etheridge, M. J.-Barnola, and D. Mazaudier (1992), Physical and climatic parameters which influence the air content in polar ice, *Earth Planet. Sci. Lett.*, *112*, 1–13, doi:10.1016/0012-821X(92)90002-D.

Nicholls, K. W., S. Østerhus, K. Makinson, and M. R. Johnson (2001), Oceanographic conditions south of Berkner Island, beneath Filchner-Ronne Ice Shelf, Antarctica, *J. Geophys. Res.*, *106*, 11,481–11,492, doi:10.1029/2000JC000350.

O'Cofaigh, C., J. A. Dowdeswell, C. S. Allen, J. F. Hiemstra, C. J. Pudsey, J. Evans, and D. J. A. Evans (2005), Flow dynamics and till genesis associated with a marine-based Antarctic palaeo-ice stream, *Quat. Sci. Rev.*, *24*, 709–740, doi:10.1016/j.quascirev.2004.10.006.

Paren, J. G., and S. Cooper (1986), George VI Ice Shelf: A temperate ice shelf, Rep. 3, pp. 62–63, Filchner-Ronne Ice Shelf Programme, Alfred-Wegener-Inst. for Polar and Mar, Res., Bremerhaven, Germany.

Pedley, M., J. G. Paren, and J. R. Potter (1988), Localized basal freezing within George VI Ice Shelf, Antarctica, *J. Glaciol.*, *34*, 71–77.

Potter, J. R., J.G. Paren (1985), Interaction between ice shelf and ocean in George VI Sound, Antarctica, in *Oceanology of the Antarctic Continental Shelf, Antarct. Res. Ser.*, vol. 43, edited by S. S. Jacobs pp. 35–58, AGU, Washington, D. C.

Potter, J. R., J. G. Paren, and J. Loynes (1984), Glaciological and oceanographic calculations of the mass balance and oxygen isotope ratio of a melting ice shelf, *J. Glaciol.*, *30*, 161–170.

Potter, J. R., M. H. Talbot, and J. G. Paren (1988), Oceanic regimes at the ice fronts of George VI Sound, Antarctic Peninsula, *Cont. Shelf Res.*, *8*, 347–362, doi:10.1016/0278-4343(88)90008-8.

Reynolds, J. M. (1981), Lakes on George VI Ice Shelf, Antarctica, *Polar Rec.*, *20*, 425–432.

Schlosser, P. (1986), Helium: A new tracer in Antarctic oceanography, *Nature*, *321*, 233–235, doi:10.1038/321233a0.

Shepherd, A., D. Wingham, and E. Rignot (2004), Warm ocean is eroding West Antarctic Ice Sheet, *Geophys. Res. Lett.*, *31*, L23402, doi:10.1029/2004GL021106.

Sugden, D. E., and C. M. Clapperton (1981), An ice-shelf moraine, George VI Sound, *Antarctica, Ann. Glaciol.*, *2*, 135–141.

Talbot, M. H. (1988), Oceanic environment of George VI Ice Shelf, Antarctic Peninsula, *Ann. Glaciol.*, *11*, 161–164.

Weiss, R. F., H. G. Östlund, and H. Craig (1979), Geochemical studies of the Weddell Sea, *Deep Sea Res., Ser. A*, *26*, 1093–1120, doi:10.1016/0198-0149(79)90059-1.

Wunsch, C. (1978), The North Atlantic general circulation west of 50°W determined by inverse methods, *Rev. Geophys.*, *16*, 583–620, doi:10.1029/RG016i004p00583.

————————
S. Jacobs, Lamont-Doherty Earth Observatory of Columbia University, Route 9W, Palisades, NY 10964, USA.

A. Jenkins, British Antarctic Survey, Natural Environment Research Council, High Cross, Madingley Road, Cambridge CB3 0ET, UK.